Electron-impact resonant vibrational excitation and dissociation processes involving vibrationally excited N_2 molecules

2014 Plasma Sources Sci. Technol. 23 065002

(http://iopscience.iop.org/0963-0252/23/6/065002)

IOP Publishing Plasma Sources Science and Technology

Plasma Sources Sci. Technol. **23** (2014) 065002 (8pp) doi:10.1088/0963-0252/23/6/065002

Electron-impact resonant vibrational excitation and dissociation processes involving vibrationally excited N_2 molecules

V Laporta[1,2], D A Little[2], R Celiberto[1,3] and J Tennyson[2]

[1] Istituto di Metodologie Inorganiche e dei Plasmi, CNR, Bari, Italy
[2] Department of Physics and Astronomy, University College London, London WC1E 6BT, UK
[3] Dipartimento di Ingegneria Civile, Ambientale, del Territorio, Edile e di Chimica, Politecnico di Bari, Italy

E-mail: vincenzo.laporta@ba.imip.cnr.it

Received 16 February 2014, revised 19 May 2014
Accepted for publication 24 June 2014
Published 7 August 2014

Abstract

Resonant vibrational excitation cross sections and the corresponding rate coefficients for electron–N_2 collisions occurring through the $N_2^-(X\,^2\Pi_g)$ resonant state are reviewed. New calculations are performed using accurate potential energy curves for the N_2 electronic ground state, taken from the literature, and for the N_2^- resonant state, obtained from R-matrix calculations. The calculations are extended to resonant excitation processes involving the N_2 ground state vibrational continuum, leading to dissociation. Electron-impact dissociation is found to be significant from higher vibrational levels. Accurate analytical fits for the complete set of the rate coefficients are provided. The behavior of the dissociative cross sections is investigated for rotationally excited N_2 molecules, with $J = 50$, 100 and 150, and for different vibrational levels.

Keywords: plasma physics, electron–molecule scattering, nitrogen

(Some figures may appear in colour only in the online journal)

1. Introduction

The nitrogen molecule plays a role of fundamental importance in many scientific and industrial activities. Typical examples are provided by air plasmas studied in a variety of fields, such as environmental research, Earth's atmosphere phenomena, combustion, and aerospace technologies [1–4]. Detailed chemistries of processes involving molecular nitrogen have been prepared for such studies [5, 6].

One of the main aspects in the formulation of a model for non-equilibrium, nitrogen-containing plasmas is represented by the description of the vibrational kinetics and its role in redistributing the internal energy of the plasma among the atomic and molecular degrees of freedom. Electron–molecule collisions, involving vibrationally excited N_2 molecules and leading to vibrational excitations, represent a central process in the kinetic evolution of the plasma. In particular, the resonant vibrational excitation (RVE) process, which occurs via the capture of the incident electron by the molecule with the formation of an unstable molecular anion, is one of the most important processes. In fact, decay of this resonance state can lead efficiently to single-quantum and multi-quantum vibrational excitations, which can strongly affect the vibrational population of the species in the plasma.

Several experimental [7–9] and theoretical [10–12] works have been devoted to studying the vibrational excitation of nitrogen by electron impact. A complete set of cross sections and related rate coefficients were recently reported in [13] (hereafter referred to as I), for the RVE process:

$$\begin{aligned} &e(\epsilon) + N_2(X\,^1\Sigma_g^+; v) \rightarrow N_2^-(X\,^2\Pi_g) \\ &\quad \rightarrow e(\epsilon') + N_2(X\,^1\Sigma_g^+; v'), \end{aligned} \tag{1}$$

where the incident electron with energy ϵ is captured by the N_2 molecule, initially in its ground electronic state $X\,^1\Sigma_g^+$ and in the vibrational level v, with the formation of the resonant state $N_2^-(X\,^2\Pi_g)$ which decays into a free electron, with energy ϵ', and a vibrationally excited molecule $N_2(X\,^1\Sigma_g^+; v')$. Cross sections $\sigma_{v,v'}(\epsilon)$ for process (1) were calculated in I

using the so-called *local-complex-potential* (LCP) model for the scattering description, using Morse-like potential energy curves [14] as input parameters, for both $N_2(X\,^1\Sigma_g^+)$ and $N_2^-(X\,^2\Pi_g)$ states. The width for the $N_2^-(X\,^2\Pi_g)$ state was based on a semi-empirical analytical function optimized to reproduce the experimental data.

In this paper we provide new RVE cross section calculations for process (1) performed using an accurate potential curve for the N_2 molecule [15]. For the N_2^- ion, the potential curve is obtained from *ab initio* calculations using the *R*-matrix method which also provides the resonance width as a function of the internuclear distance. The cross section calculations are extended to the RVE process ending in the vibrational continuum of the ground state [16]. The repulsive nature of the curve induces the separation of the nuclei, so the molecule undergoes dissociation with the production of two stable nitrogen atoms in their lowest electronic state. The resonant dissociation process can then be represented as

$$\begin{aligned} &e(\epsilon) + N_2(X\,^1\Sigma_g^+;\, v,\, J) \rightarrow N_2^-(X\,^2\Pi_g) \\ &\quad \rightarrow e(\epsilon') + N_2(X\,^1\Sigma_g^+; \text{continuum}) \rightarrow e(\epsilon') + 2\,N(^4S). \quad (2) \end{aligned}$$

This dissociative channel is particularly important in plasma kinetics because, in non-equilibrium conditions, it can compete with the dissociation from heavy species collisions [17–19].

The cross sections for processes (1) and (2) have been obtained as a function of the incident electron energy and for all the initial vibrational levels v by adopting the LCP model, and then used for the calculation of the corresponding rate coefficients, assuming a Maxwell distribution for electrons, according to the equation

$$\kappa_{v,v'}(T) = \sqrt{\frac{8}{m_e\,\pi}} \left(\frac{1}{T}\right)^{3/2} \int_{\epsilon_{th}}^{\infty} d\epsilon\, \epsilon \cdot e^{-\frac{\epsilon}{T}} \cdot \sigma_{v,v'}(\epsilon), \quad (3)$$

where m_e is the electron mass and the temperature T is expressed in energy units. It is worth noting that equation (3) is no longer valid in non-equilibrium conditions. Cross sections are also studied for some values of the rotational quantum number, namely $J = 50$, 100 and 150.

The paper is organized as follows: in the next section the *R*-matrix calculations are described and the main equations of the LCP model are shown; the results are presented and commented on in section 3, while in section 4, a brief summary concludes the work.

2. The theoretical model

2.1. The *R*-matrix method

Electron–N_2 calculations were performed using the *R*-matrix method as implemented in the UKRMol codes [20]. For details of this methodology we refer the reader to the review by one of us [21]. Put simply, the *R*-matrix method divides space into an inner region defined by a sphere centered on the target center of mass. This sphere, here taken to be of size 10 a_0, is assumed to enclose the entire charge cloud of the N-electron target. Within the sphere the wavefunction of the $(N+1)$-electron scattering problem is built from target wavefunctions and extra functions designed to represent the scattering continuum. Here, and in general, this problem is built around using the complete active space (CAS) configuration interaction (CI) representation of the target wavefunction for which a particularly efficient purpose-built algorithm is used [22]. In the outer region, the interaction of the scattering electron with the target is assumed to occur only via diagonal and off-diagonal multipole moments of the target. While the inner region problem only has to be solved once for each total scattering symmetry, the much faster outer region problem is solved at each scattering energy of interest. Below we give specific details for the present calculation.

Target calculations used the cc-pVQZ Gaussian-type orbital (GTO) basis set due to Dunning. Orbitals for the N_2 target were generated using multi-configuration self-consistent field (MCSCF) calculations run in MOLPRO [23]. The CAS used in these calculations and to define the target wavefunction in the *R*-matrix calculations is given by

$$(1\sigma_g,\, 1\sigma_u)^4 (2\sigma_g,\, 2\sigma_u,\, 1\pi_u,\, 3\sigma_g,\, 1\pi_g,\, 3\sigma_u)^{10}.$$

A total of 128 target states were generated (eight per symmetry) of which the 49 lowest in energy were retained for the inner region calculation. Calculations were performed for 100 geometries from 0.8 to 3.77 Å in steps of 0.03 Å.

For the scattering calculations, $(4\sigma_g,\, 5\sigma_g,\, 4\sigma_u,\, 2\pi_u,\, 2\pi_g,\, 1\delta_g)$ target orbitals were retained. These were augmented with a continuum orbital containing up to g ($l = 4$) functions represented by a GTO expansion at the target center of mass [24]. These were orthogonalized to the target orbitals with a deletion threshold set to 10^{-7} [25]. The target times continuum configurations were augmented with the following short-range functions based on the use of target orbitals:

$$(1\sigma_g,\, 1\sigma_u)^4 (2\sigma_g,\, 2\sigma_u,\, 1\pi_u,\, 3\sigma_g,\, 1\pi_g,\, 3\sigma_u)^{11},$$

which involves placing the scattering electron in the target CAS, and

$$\begin{aligned} &(1\sigma_g,\, 1\sigma_u)^4 (2\sigma_g,\, 2\sigma_u,\, 1\pi_u,\, 3\sigma_g,\, 1\pi_g,\, 3\sigma_u)^{10} \\ &\quad \times (2\pi_u,\, 4\sigma_g,\, 5\sigma_g,\, 2\pi_g,\, 1\delta_g,\, 4\sigma_u)^1, \end{aligned}$$

where the scattering electron enters, with the otherwise unoccupied target virtual. These configurations were not constrained by contracting to target CI wavefunctions [26].

For computational efficiency, only the lowest two target states, $X\,^1\Sigma_g^+$ and $A\,^3\Sigma_u^+$, were retained in the outer region calculation. This problem was solved by propagating the *R*-matrix to 100.1 a_0 and then using a Gailitis expansion. The resulting eigenphases were searched for a resonance which was fitted to a Breit–Wigner form using an automated procedure [27]. These calculations concentrated on the $^2\Pi_g$ total symmetry, as this is the symmetry of the well known, low-lying N_2^- shape resonance.

The $N_2(X\,^1\Sigma_g^+)$ potential energy curve is taken from Le Roy *et al* [15] who obtained it from an accurate fit to spectroscopic data. The resulting potential curves for both N_2 and N_2^-, along with the corresponding width $\Gamma(R)$, are shown in figures 1(*a*) and (*b*) respectively. The $N_2^-(X\,^2\Pi_g)$ resonance

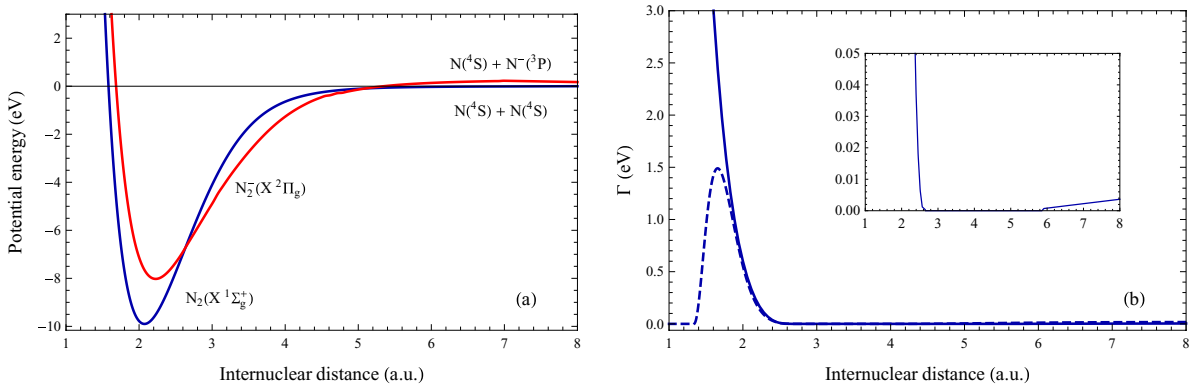

Figure 1. (*a*) Potential energy curves for $N_2(X\,^1\Sigma_g^+)$ and $N_2^-(X\,^2\Pi_g)$ and (*b*) resonance width $\Gamma(R)$ as a function of the internuclear distance: solid line, this work; dashed line, the phenomenological width calculated in I. The inset plot shows a magnified view of our resonance width ($\Gamma(R) \leqslant 0.05$ eV).

Table 1. Equilibrium distance (R_e), dissociation energy (D_e), vertical excitation (T_e), resonance position calculated at the N_2 equilibrium bond length (RP) and electronic affinity (EA) for the N_2 and N_2^- ground state potential energy curves.

	$N_2(X\,^1\Sigma_g^+)$	$N_2^-(X\,^2\Pi_g)$
R_e (a_0)	2.07	2.23
D_e (eV)	9.89	8.22
T_e (eV)	0	1.97
RP (eV)	—	2.34
EA (eV)	—	−0.30

curve crosses $N_2(X\,^1\Sigma_g^+)$ at ∼2.657 a_0 and ∼5.132 a_0. In this intermediate region the molecular ion N_2^- becomes stable and the resonance width vanishes, as is shown in the inset box in figure 1(*b*). For geometries where N_2^- is bound, the position of the bound state was determined using the same model and by performing negative energy scattering calculations [28]. Table 1 reports some relevant spectroscopical parameters for the two potentials.

2.2. The vibrational dynamics

In this section the main equations for the description of the vibrational dynamics of the collision in the framework of the LCP model are summarized. Extensive theoretical formulations of electron–molecule resonant scattering can be found elsewhere [29–31].

The cross sections for the RVE processes in (1), with incoming electron energy ϵ, were calculated using the following formula:

$$\sigma_{v,v'}(\epsilon) = g\,\frac{64\,\pi^5\,m^2}{\hbar^4}\,\frac{k'}{k}\,|\mathcal{T}_{v,v'}(\epsilon)|^2, \tag{4}$$

where k (k') is the ingoing (outgoing) electron momentum, g contains the spin-statistic weight factors and v (v') represents the bound initial (final) nitrogen vibrational levels. $\mathcal{T}_{v,v'}$ is the T-matrix of the process. The definition in equation (4) can be extended to the resonant dissociation process (2) by considering that the final vibrational energy falls now in the continuum spectrum of the N_2 ground state potential. The right-hand side of equation (4) retains the same form, but it expresses now the energy-differential cross section $\mathrm{d}\sigma_{v,\epsilon'}(\epsilon)/\mathrm{d}\epsilon'$. An extra integration over the final continuum levels of energy ϵ' is thus required according to [16, 32, 33]

$$\sigma_v(\epsilon) = \int_{\epsilon_{\rm th}}^{\epsilon_{\rm max}} \mathrm{d}\epsilon'\,\frac{\mathrm{d}\sigma_{v,\epsilon'}(\epsilon)}{\mathrm{d}\epsilon'}, \tag{5}$$

where $\epsilon_{\rm th}$ is the dissociation threshold. In our calculations the integration over the continuum has been extended up to $\epsilon_{\rm max} = \epsilon_{\rm th} + 10$ eV.

According to the LCP model of Fano and Bardsley's theory of resonant scattering [29, 34], the $\mathcal{T}$-matrix in equation (4) is given by

$$\mathcal{T}_{v,v'}(\epsilon) = \langle \chi_{v'}|V_{\mathrm{d}k'}|\xi\rangle, \tag{6}$$

where $\xi(R)$ is the resonant state nuclear wavefunction, a solution of the Schrödinger-like equation

$$\left(T_N + V^- - \frac{\mathrm{i}}{2}\Gamma - E\right)\xi(R) = -V_{\mathrm{d}k}\,\chi_v, \tag{7}$$

with total energy $E = \epsilon + \epsilon_v$ and for the resonant complex potential $(V^-(R), \Gamma(R))$. Moreover, $\chi_{v\,(v')}(R)$ is the initial (final) vibrational wavefunction, with the corresponding eigenvalues $\epsilon_{v\,(v')}$, belonging to the N_2 ground state potential energy, denoted by $V^0(R)$, and T_N is the nuclear operator. Finally, $V_{\mathrm{d}k}$ is the continuum–discrete coupling potential given by

$$V_{\mathrm{d}k} = \sqrt{\frac{1}{4\pi}\,\frac{\Gamma(R)}{2\pi}\,\frac{\hbar^2}{m\,k(R)}}, \tag{8}$$

where $k(R) = \sqrt{2m[V^-(R) - V^0(R)]}/\hbar$.

3. Results and discussion

The potential curve for the N_2 ground state, used in the present calculations, supports 59 vibrational levels, which are reported in table 2. This is fewer than the 68 levels found for the Morse curve adopted in I, which implies that there is not a one-to-one correspondence in the energy eigenvalues for the same v in the two sets of calculations. However, the energies of the first few levels do not show large differences compared with

Table 2. Vibrational levels given by the N_2 potential energy curve [15] counted from the lowest level $v = 0$, which has a zero-point energy of 0.146 eV.

v	ϵ_v (eV)	v	ϵ_v (eV)	v	ϵ_v (eV)	v	ϵ_v (eV)
0	0.000	15	3.959	30	7.084	45	9.163
1	0.288	16	4.195	31	7.260	46	9.252
2	0.573	17	4.426	32	7.430	47	9.335
3	0.855	18	4.654	33	7.596	48	9.409
4	1.133	19	4.878	34	7.757	49	9.476
5	1.408	20	5.099	35	7.913	50	9.535
6	1.679	21	5.315	36	8.064	51	9.587
7	1.947	22	5.528	37	8.210	52	9.631
8	2.211	23	5.737	38	8.350	53	9.667
9	2.471	24	5.942	39	8.485	54	9.696
10	2.728	25	6.143	40	8.614	55	9.717
11	2.982	26	6.339	41	8.737	56	9.732
12	3.232	27	6.532	42	8.853	57	9.742
13	3.478	28	6.721	43	8.963	58	9.748
14	3.720	29	6.905	44	9.067		

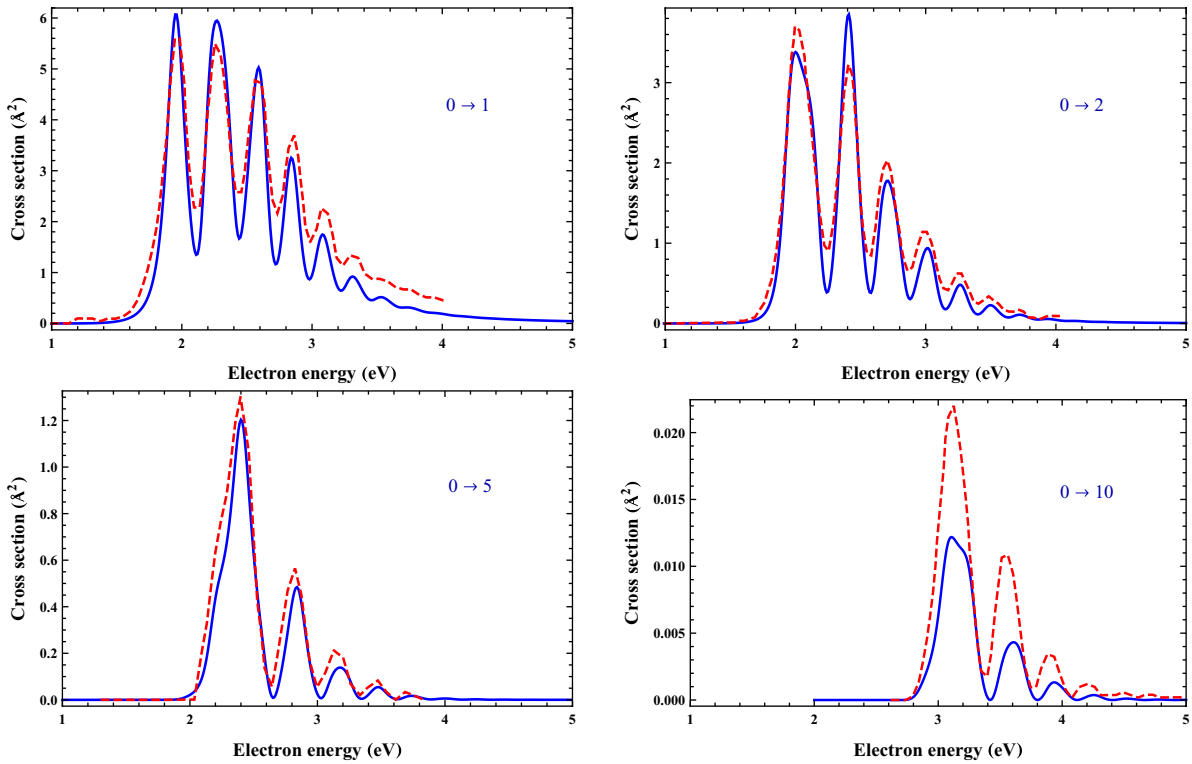

Figure 2. Cross section comparison between the present calculations (full blue line) and the measurements (dashed red line) of Allan [7]. The experimental data have an estimated uncertainty of ±20%.

those of I and so the updated cross sections remain practically the same. This means that the good agreement between the calculated cross sections and the experimental measurements observed in I is retained in the present results, as can be seen in figures 2 and 3 where the new theoretical results are compared with the experimental data of Allan [7] and Vićić *et al* [8] respectively.

Figure 4 compares also the calculated total cross sections with the experimental data of [35, 36]. Our theoretical curve was obtained as a sum over the final vibrational resonant cross sections, in the resonance region (∼2 eV), and the non-resonant background contribution $\sigma^{bg}(\epsilon)$, as

$$\sigma^{\text{tot}}(\epsilon) = \sum_{v'} \sigma^{\text{res}}_{0\to v'}(\epsilon) + \sigma^{bg}(\epsilon), \tag{9}$$

where $\sigma^{bg}(\epsilon)$ was calculated using the R-matrix method for evaluating the T-matrix at the equilibrium internuclear distance for all symmetries except the resonant $^2\Pi_g$ one. Above ∼2.5 eV our cross sections are in good agreement with the observed ones. At lower energies the background is too high. This is due to the lack of polarization effects in the R-matrix calculation which become increasingly important at very low collision energies. It is possible to include these effects in the calculation but only by making the calculation significantly more expensive [37]. In the resonance region below ∼2.5 eV, the theoretical peaks are higher than the experimental ones and show a small shift which is, however, not present in the comparison with the inelastic cases shown in figures 2 and 3.

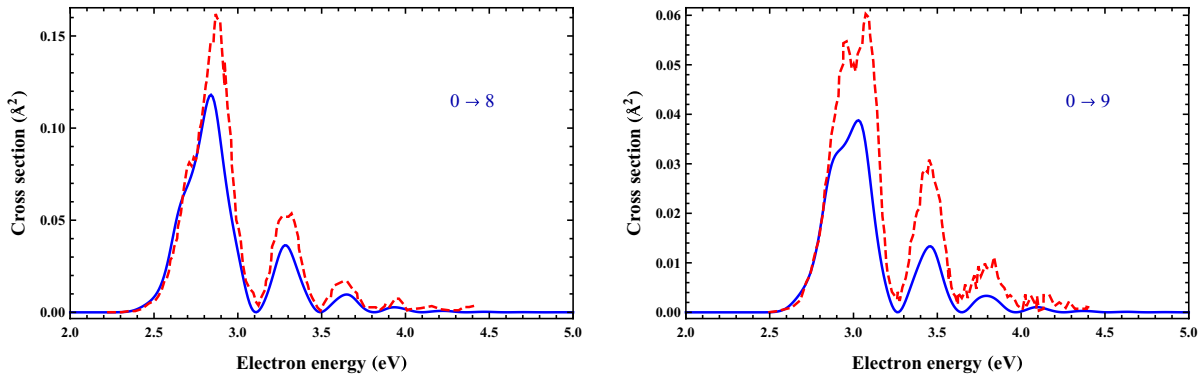

Figure 3. Cross section comparison between the present calculations (full blue line) and the measurements of Vićić *et al* [8].

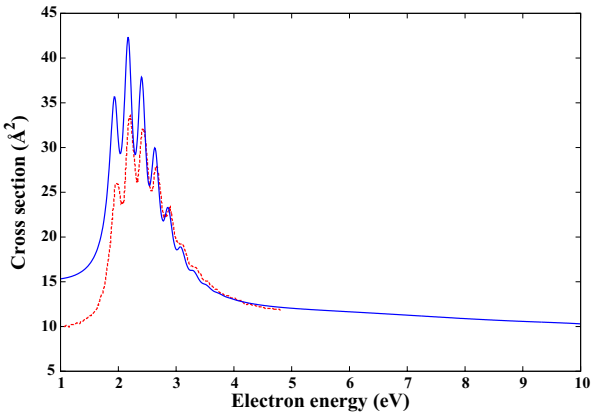

Figure 4. Comparison between calculated and measured total cross sections (see the text). Present theoretical results (full blue line) and experimental data (dashed red line) [35, 36].

There is an important difference between the resonance widths shown in figure 1(*b*). The width calculated *ab initio* using the *R*-matrix method (solid line) shows a monotonic increase toward short bond lengths which contrasts with the bell-shaped behavior of the semi-empirical $\Gamma(R)$ obtained in I (dashed line). However, the two curves overlap for bond lengths greater than 1.8 a_0, which covers the Franck–Condon region for the transitions from the vibrational ground state. This explains the absence of any substantial differences between the present calculations and those reported in I for the corresponding vibrational excitation cross sections.

Figure 5 shows a set of the new calculated RVE cross sections and the corresponding rate coefficients for the $v \rightarrow v + 1$ single-quantum transitions, which play a prominent role in the plasma vibrational kinetics. The cross section curves displayed are labeled with the selected values of the vibrational quantum number v. As extensively discussed in paper I, the sharp peaks in the cross sections shown in figures 2–5 are due to the well know boomerang oscillations and their position corresponds to the energy of the resonant vibrational levels. For high energies the cross sections drop down by several orders of magnitude, relative to their peak value, so in the integration of the rate coefficients in equation (3) they were considered negligible beyond 15 eV.

The cross sections for the dissociative process (2), calculated by equation (5), are shown in figure 6 for some initial vibrational levels as a function of the incident electron energy. An immediate conclusion which can be drawn from figure 6(*a*), where the plots are represented on a log y scale, is that the cross sections for low levels ($v \lesssim 20$) are extremely small, so the role of the corresponding dissociative processes in plasma kinetics can be expected to be negligible. For higher levels however, the cross sections tend to saturate above 10^{-2} Å^2, which implies that in strong non-equilibrium plasma conditions, that is when the higher levels are overpopulated with respect to the Boltzmann distribution, the dissociative processes, starting from these levels, will play a major role. Figure 6(*b*) shows the cross sections on a linear scale for some v values ranging from 0 through 30. All the curves exhibit two large, sharp peaks and a structure of smaller intensity very close to the apparent threshold. These features are also present in all the calculated cross sections, as can be seen in figure 6(*c*). Inspection of the numerical values shows that the peak positions coincide with some of the vibrational eigenvalues of the $N_2^-(X\,^2\Pi_g)$ resonant state, placed inside the electronic affinity gap, of |0.30| eV (see table 1), between the asymptotic limits of the $N_2(X\,^1\Sigma_g)$ and $N_2^-(X\,^2\Pi_g)$ potential curves. We found, in this interval, twelve resonant vibrational levels which are the only 'bound' states that can lead to dissociation. These levels, in fact, can enter in resonance with the continuum of the N_2 ground state, while above the N_2^- dissociation limit, in contrast, the interaction of the two continua occurs.

As v is increased, the threshold of the resonant dissociation process is lowered, so the cross section peaks in figure 6(*b*) move toward lower energies. On the other side of the peaks and for large incident energies, some oscillation is observed in the curves. This is due to numerical noise. In fact, the very small absolute values of the low-level cross sections ($\sim 10^{-8}$ Å^2) imply a reduced accuracy in the calculations, so numerical instabilities become evident. For $v = 8, 9, 10$ the corresponding cross sections ($\sim 10^{-7}$ Å^2; not shown) are even larger, while for $v \gtrsim 20$, for which the cross sections become significantly large, the oscillations remain confined to very small values and disappear from the plots.

Figure 6(*c*) shows cross sections for some initial levels with $v \geqslant 35$; besides the sharp peaks already discussed, there is also a broad maximum arising at about 5 eV, whose intensity grows with the vibrational quantum number up to $v = 50$ then decreases for $v = 53$ and 55 (dashed lines). This maximum

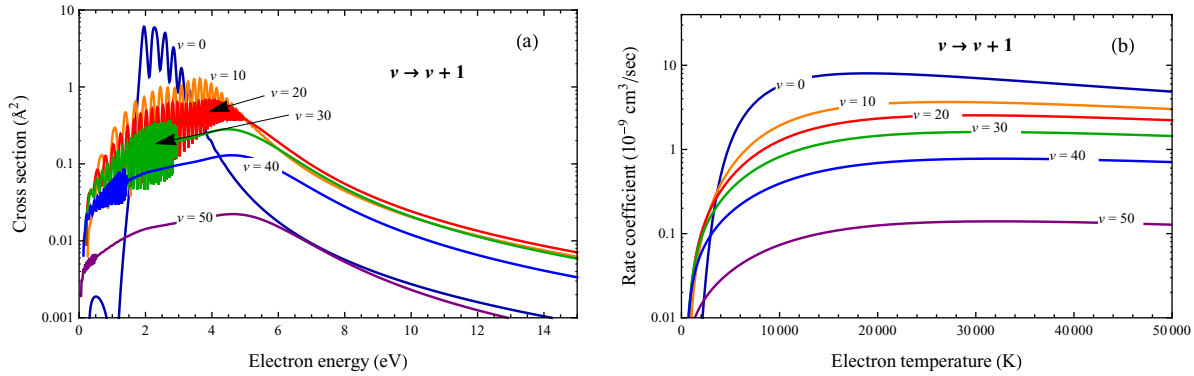

Figure 5. (*a*) Electron–N_2 RVE cross sections and (*b*) the corresponding rate coefficients for selected single-quantum transitions.

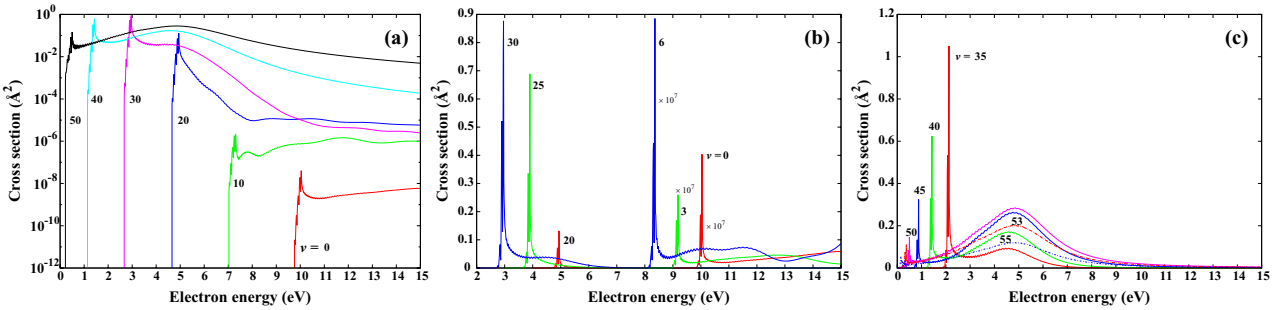

Figure 6. Resonant electron–N_2 dissociation cross sections for some initial vibrational levels, as indicated in the figure, and for $J = 0$. (*a*) gives plots on a log *y*-scale. In (*b*) the cross sections for $v = 0$, 3 and 6 have been multiplied by 10^7, as shown. In (*c*) the dashed lines ($v = 53$ and 55) indicate a decreasing trend for the corresponding cross sections.

occurs when the N_2 vibrational states lie in the continuum spectrum of the N_2^- ion and is therefore due to the interplay of the Franck–Condon overlap between the N_2 and N_2^- bound and continuum levels respectively, during the electron capture, and that of the two continua in the emission process.

Rate coefficients were also calculated for process (2) using equation (3) and the corresponding dissociative cross sections. Figure 7 shows the rates as a function of the electron temperature for the initial vibrational levels $v = 20$, 30, 40 and 50. These rates follow the same trend as the cross sections, being negligible for low $v(\lesssim 20)$ and becoming significant for higher vibrational levels. Likely in the RVE case, the dissociation cross sections decrease rapidly as a function of the electron energy, so again we extended the integration in the calculation of the rate coefficients up to 15 eV.

The rates can be easily and accurately reproduced using the following analytical expression:

$$\kappa_v(T) = \kappa_v^{\max} \left(\frac{T_v^{\max}}{T} \right)^{3/2} \mathrm{e}^{-\frac{T_v^{\max}}{T}}, \qquad (10)$$

already successfully tested for electron–H_2 scattering [38]. The equation requires only two parameters, $T_v^{\max}$ and $\kappa_v^{\max}$, which are the coordinates of the maximum value of the calculated rates for each level v. Equation (10) works quite well for all v but the last three values ($v = 56$, 57 and 58), as the corresponding rates show some irregularity, probably coming from the related cross sections which, for these very high levels, suffer from reduced numerical accuracy. $T_v^{\max}$ and $\kappa_v^{\max}$ are provided here as supplementary material for both dissociative

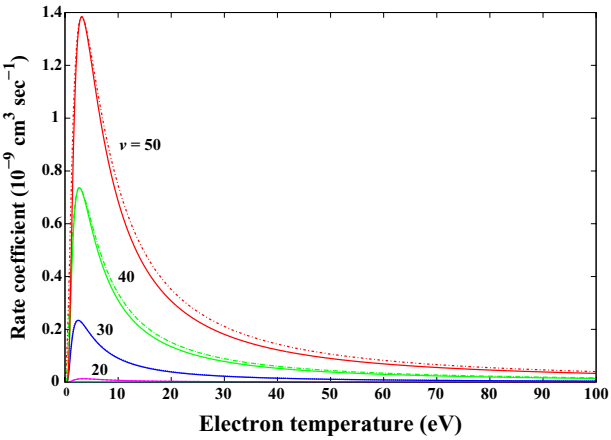

Figure 7. Calculated (full lines) and fitted (dashed lines) rate coefficients for resonant dissociation as a function of the electron temperature and for the vibrational levels indicated.

($0 \leqslant v \leqslant 55$) and RVE processes ($0 \leqslant v \leqslant v' \leqslant 55$). The RVE rates for $v \geqslant v'$ can be obtained from the detailed balance [39].

We also investigated the behavior of the dissociative process as a function of the rotational state. Figure 8 shows the cross sections for $J = 50$, 100 and 150 and for varying v. In calculating these cross sections we have started the integration in equation (5) above the centrifugal barrier created in the N_2 potential curve by the nuclear rotation, instead of from the dissociation energy ϵ_{th}. This barrier, in fact, can support a number of quasi-bound states which can lead to dissociation

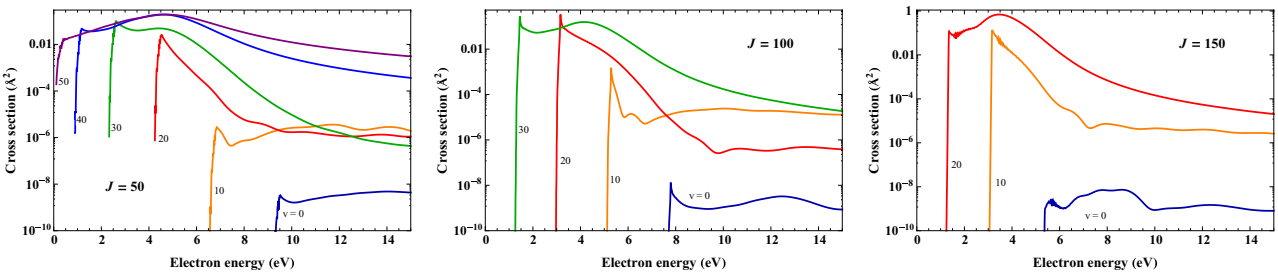

Figure 8. Resonant dissociation cross sections as a function of the electron energy, for some vibrational levels and for $J = 50$, $J = 100$ and $J = 150$.

by tunneling. We have assumed that the contribution of these metastable states, if they exist, to the dissociation is small compared to the process occurring from the repulsive part of the potential curve, due to the delay accumulated by the nuclei inside the barrier. Figure 8 shows, for a given J, that again the cross sections present structures near the threshold and become significant values for high vibrational levels, comparable in magnitude with those for $J = 0$.

4. Conclusions

In this article we update the resonant vibrational excitation cross sections and rate coefficients reported in I. Our new calculations use accurate potential energies for both N_2 and N_2^- ground states. For the neutral molecule we use the experimentally derived potential curves [15], while for the N_2^- resonant state we perform new calculations using the R-matrix method, obtaining also the resonance width as a function of the bond length.

We extend the cross section calculations to the study of dissociative resonant vibrational excitations using the same model. The energy-dependent cross section curves obtained show some sharp peaks close to the process threshold, which are caused by resonant bound states located in between the dissociation limits of the N_2 and N_2^- molecules. Above these levels, resonant coupling occurs among the two continua of the neutral and ionic species. The dissociation cross sections are of very small values for low initial vibrational levels, but become important for high $v(\gtrsim 20)$. The same behavior is shown by the corresponding rate coefficients. For these last quantities, as well as for the RVE rates, a two-parameter analytical fitting expression has been formulated for their rapid and accurate evaluation, which should be useful for practical applications. Finally, cross sections for $J = 50$, 100 and 150, and for varying v, have been also investigated. Their behavior, as well as their order of magnitude, is comparable to those for the cross sections for $J = 0$.

As already stressed previously, the resonant dissociative cross sections starting from the $v = 0$ level are particularly small. This can be better seen in comparison with the experimental measurements for $N_2(v = 0)$ reported by Cosby [40], which found that the dominant contribution to dissociation comes from electronically excited states leading to $N(^2D) + N(^4S)$. However, in nitrogen plasmas, exposed to high temperature and electric fields, the contribution coming from the resonant dissociation from all the vibrational levels is comparable with that of the dominant kinetic mechanism of dissociation induced by vibrational quanta exchange, which gradually excites the molecules up to the vibrational continuum (the so-called *'pure-vibrational mechanism'*) as discussed in [41].

The complete set of cross sections and the corresponding rate constants can be downloaded from the 'Phys4Entry' database [42] and the parameters of the fit in equation (10) can be found as supplementary material of this paper.

Acknowledgments

This work received funding from the European Community's Seventh Framework Program (FP7/2007-2013) under grant agreement No 242311. One of the authors (DAL) would like to also express gratitude for the support from Themisys Limited, supporting a studentship. The authors wish to thank Drs W M Huo, R Jaffe and D W Schwenke (NASA Ames Research Center) for providing the N_2 potential energy curve from [15].

References

[1] Gordillo-Vàzquez F J 2008 *J. Phys. D: Appl. Phys.* **41** 234016
[2] Shang J S and Surzhikov S T 2012 *Prog. Aerospace Sci.* **53** 46
[3] Laporta V and Bruno D 2013 *J. Chem. Phys.* **138** 104319
[4] Capitelli M, Celiberto R, Colonna G, Laporta V and Tennyson J 2013 *Int. Conf. on Phenomena in Ionized Gases XXXI ICPIG (Granada (ES), Spain)*
[5] Bultel A and Annaloro J 2013 *Plasma Sources Sci. Technol.* **22** 025008
[6] Dutuit O *et al* 2013 *Astrophys. J. Suppl.* **204** 20
[7] Allan M 1985 *J. Phys. B: At. Mol. Opt. Phys.* **18** 4511
[8] Vicic M, Poparic G and Belic D S 1996 *J. Phys. B: At. Mol. Opt. Phys.* **29** 1273
[9] Ristic M, Poparic G B and Belic D S 2007 *Chem. Phys.* **331** 410–6
[10] Schneider B I, Le Dourneuf M and Vo Ky Lan 1979 *Phys. Rev. Lett.* **43** 1926–9
[11] Huo W M, Gibson T L, Lima M A P and McKoy V 1987 *Phys. Rev.* A **36** 1632–41
[12] Mihajlov A A, Stojanovic V D and Petrovic Z Lj 1999 *J. Phys. D: Appl. Phys.* **32** 2620
[13] Laporta V, Celiberto R and Wadehra J M 2012 *Plasma Sources Sci. Technol.* **21** 055018
[14] Gilmore F R 1965 *J. Quant. Spectrosc. Radiat. Transfer* **5** 369–89
[15] Le Roy R J, Huang Y and Jary C 2006 *J. Chem. Phys.* **125** 164310
[16] Atems D E and Wadehra J M 1993 *J. Phys. B: At. Mol. Opt. Phys.* **26** L759

[17] Panesi M, Jaffe R L, Schwenke D W and Magin T E 2013 *J. Chem. Phys.* **138** 044312
[18] Esposito F, Armenise I and Capitelli M 2006 *Chem. Phys.* **331** 1–8
[19] Adamovich I V 2014 *Phys. Fluids* **26** 046102
[20] Carr J M, Galiatsatos P G, Gorfinkiel J D, Harvey A G, Lysaght M A, Madden D, Masin Z, Plummer M and Tennyson J 2012 *Eur. Phys. J.* D **66** 58
[21] Tennyson J 2010 *Phys. Rep.* **491** 29–76
[22] Tennyson J 1996 *J. Phys. B: At. Mol. Opt. Phys.* **29** 1817–28
[23] Werner H-J *et al* 2010 MOLPRO, version 2010 .1, a package of ab initio programs
[24] Faure A, Gorfinkiel J D, Morgan L A and Tennyson J 2002 *Comput. Phys. Commun.* **144** 224–41
[25] Morgan L A, Tennyson J and Gillan C J 1998 *Comput. Phys. Commun.* **114** 120–8
[26] Tennyson J 1996 *J. Phys. B: At. Mol. Opt. Phys.* **29** 6185–201
[27] Tennyson J and Noble C J 1984 *Comput. Phys. Commun.* **33** 421–4
[28] Sarpal B K, Branchett S E, Tennyson J and Morgan L A 1991 *J. Phys. B: At. Mol. Opt. Phys.* **24** 3685–99
[29] Bardsley J N and Mandl F 1968 *Rep. Prog. Phys.* **31** 471
[30] Domcke W 1991 *Phys. Rep.* **208** 97–188
[31] Wadehra J M 1986 *Nonequilibrium Vibrational Kinetics* (*Topics in Current Physics* vol 39) ed M Capitelli (Berlin: Springer)
[32] Stibbe D T and Tennyson J 1998 *New J. Phys.* **1** 2
[33] Celiberto R, Laricchiuta A, Lamanna U T, Janev R K and Capitelli M 1999 *Phys. Rev.* **60** 2091–103
[34] Bardlsey J N 1968 *J . Phys. B: At. Mol. Phys.* **1** 349
[35] Kennerly R E 1980 *Phys. Rev.* A **21** 1876
[36] Itikawa Y 2006 *J. Phys. Chem. Ref. Data* **35** 31
[37] Brigg W J, Tennyson J and Plummer M 2014 *J. Phys. B: At. Mol. Opt. Phys.* submitted
[38] Celiberto R, Janev R K, Laporta V, Tennyson J and Wadehra J M 2013 *Phys. Rev.* A **88** 062701
[39] Celiberto R, Janev R K and Reiter D 2012 *Plasma Phys. Control. Fusion* **54** 035012
[40] Cosby P C 1993 *J. Chem. Phys.* **98** 9544
[41] Capitelli M, Colonna G, D'Ammando G, Laporta V and Laricchiuta A 2014 *Chem. Phys.* **438** 31–6
[42] Database of the European union phys4entry project 2012 http://users.ba.cnr.it/imip/cscpal38/phys4entry/database.html